Journal of Hydrology 623 (2023) 129814

Contents lists available at ScienceDirect

Journal of Hydrology

journal homepage: www.elsevier.com/locate/jhydrol

Research papers

Image-based machine learning for monitoring the dynamics of deltaic islands in the Atchafalaya River Delta Complex between 1991 and 2019

Jiangjie Yang [a], Zhijun Dai [a,b,1,*], Yaying Lou [a], Xuefei Mei [a,1,*], Sergio Fagherazzi [c]

[a] State Key Laboratory of Estuarine and Coastal Research, East China Normal University, Shanghai 200062, China
[b] Laboratory for Marine Geology, Qingdao National Laboratory for Marine Science and Technology, Qingdao 266061, Shandong, China
[c] Department of Earth and Environment, Boston University, Boston 02215, MA, USA

ARTICLE INFO

This manuscript was handled by Marco Borga, Editor-in-Chief, with the assistance of Marco Toffolon, Associate Editor

Keywords:
Morphodynamics
Deltaic islands
Atchafalaya River Delta Complex
Machine learning

ABSTRACT

Deltaic islands are distinct hydro-environmental zones with global significance in food security, biodiversity conservation, and fishery industry. These islands are the fundamental building blocks of many river deltas. However, deltaic islands are facing severe challenges due to intensive anthropogenic activities, sea level rise, and climate change. In this study, dynamic changes of deltaic islands in Wax Lake Delta (WLD) and Atchafalaya Delta (AD), part of the Atchafalaya River Delta Complex (ARDC) in Louisiana, USA, were quantified based on remote sensing images from 1991 to 2019 through a machine learning method. Results indicate a significant increase in deltaic islands area for the whole ARDC at a rate of 1.29 km^2/yr, with local expansion rates of 0.60 km^2/yr for WLD and 0.69 km^2/yr for AD. All three parts of the WLD naturally prograded seaward, with the western part (WP) and central part (CP) expanding southwestward to the sea, while the eastern part (EP) prograding southeastwards. Differently from WLD, the three parts of AD irregularly expanded seaward under the impacts of anthropogenic activities. The WP and CP of the AD expanded respectively northwestwards and southwestwards, while the EP remained stable. Different drivers dominate the growth of deltaic islands in the WLD and AD. Specifically, fluvial suspended sediment discharge and peak flow events were responsible for the shift in the spatial evolution of WLD, while dredging and sediment disposal contributed to the expansion of AD. Tropical storms with different intensity and landing locations caused short-term deltaic island erosion or expansion. Tropical storms mainly generated erosion on the deltaic islands of the WLD, while causing transient erosion or siltation on the deltaic islands of the AD. In addition, high-intensity hurricanes that made landfall east of the deltas caused more erosion in the AD. Finally, sea level rise, at the current rate of 8.17 mm/yr, will not pose a threat to the deltaic island of WLD, while the eastern part of AD may be at risk of drowning. This study recognizes the complexity of factors influencing the growth of deltaic islands, suggesting that quantitative studies on the deltaic island extent are of critical for the restoration and sustainable management of the Mississippi River Delta and other deltas around the world.

1. Introduction

Deltaic islands, which form at the mouth of distributary channels, are the fundamental building blocks that create deltaic land in many river deltas (Shaw et al., 2014; Nardin et al., 2016; Sendrowski et al., 2016). These islands are active and vulnerable hydro-environmental zones with regional significance in terms of biodiversity, conservation, and protections of coastal communities (Costanza et al., 2008; Fagherazzi et al., 2015). Unfortunately, deltaic islands are facing severe challenges around the world because of sea level rise (SLR), storm erosion, and a dramatic reduction in riverine sediment load (Syvitski et al., 2009; Nienhuis et al., 2020; Dai et al., 2013, 2021). As a result, deltaic islands morphodynamics and associated disturbances by natural and anthropogenic drivers have attracted worldwide attention in recent years (Ericson et al., 2006; Syvitski et al., 2009; Fagherazzi et al., 2015; Nardin et al., 2016).

Deltaic islands are formed by continuous deposition and vertical accretion of a mouth bar, and can efficiently contribute to the expansion of fluvial deltas thus expanding coastal regions (Fagherazzi et al., 2015; Nardin et al., 2016; Zhou et al., 2020). Fagherazzi et al. (2015) found

* Corresponding authors.
E-mail addresses: zjdai@sklec.ecnu.edu.cn (Z. Dai), xfmei@geo.ecnu.edu.cn (X. Mei).
[1] These are equally contribution.

https://doi.org/10.1016/j.jhydrol.2023.129814
Received 9 January 2023; Received in revised form 30 May 2023; Accepted 11 June 2023
Available online 20 June 2023

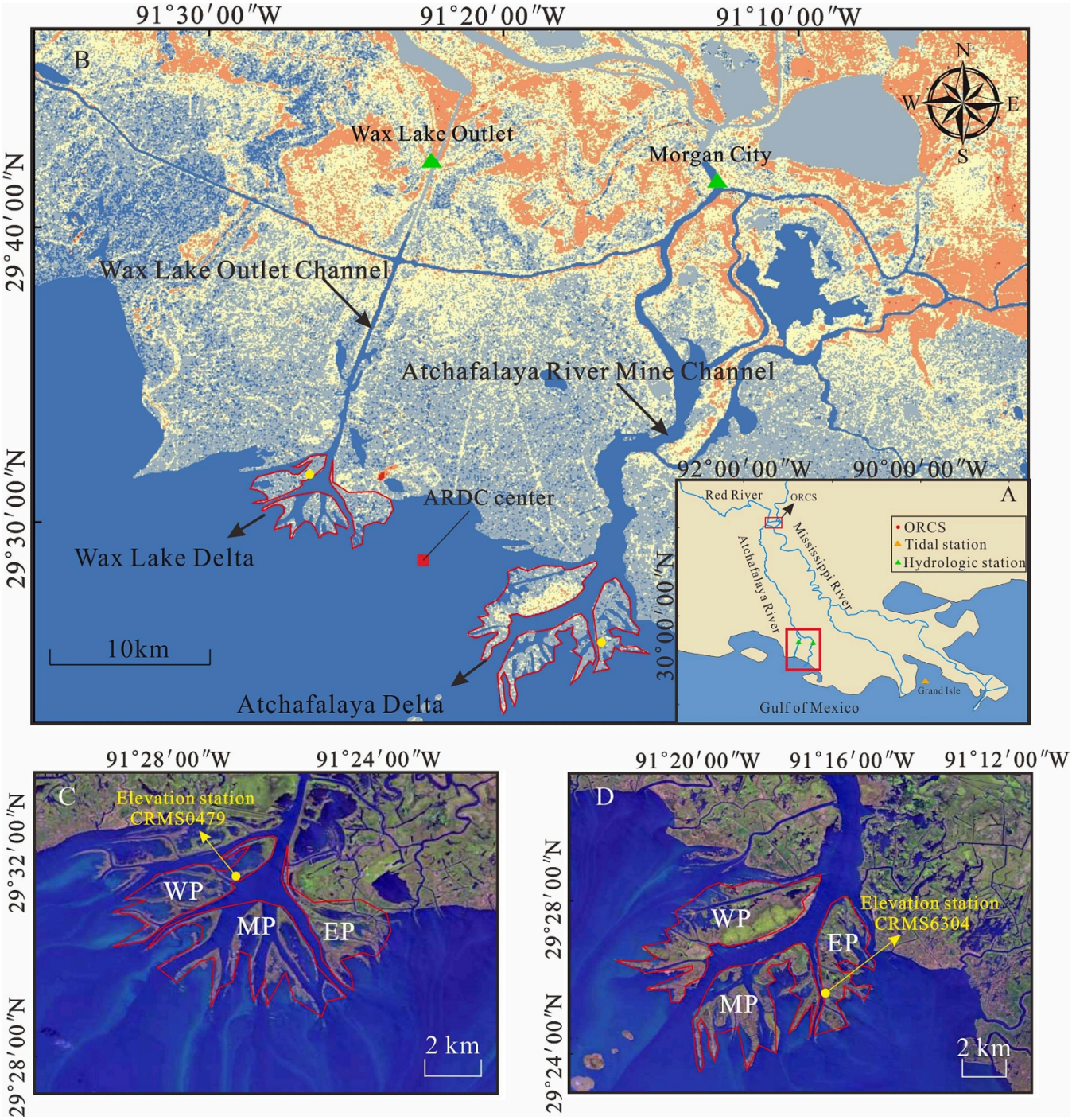

Fig. 1. Study area. A. Lower Mississippi River; B. Lower Atchafalaya River. C. The WLD is divided into three parts: western part (WP), central part (CP) and eastern part (EP); D. The AD is also divided into three parts: western part (WP), central part (CP) and eastern part (EP). ARDC center is defined by the point of equal distance of WLD and AD.

that initially, mouth bars form by sedimentation associated with turbulent jet expansion. Nardin et al. (2016) discovered that deposition on emergent deltaic islands is influenced by vegetation, and that intermediate vegetation heights and densities may increase sedimentation and provide a stabilizing cover that creates more resilient deltas. In addition, many studies indicate that the decrease in riverine sediment, saltwater intrusion, intensified storm-surge activities, and sea level rise have a significant impact on the evolution of river mouth bars, thus affecting the development of deltaic islands (Reeve and Karunarathna, 2009; Syvitski et al., 2009; Dai et al., 2013; Anthony et al.,2015). Reeve and Karunarathna (2009) suggested that mouth bars would remain in a stable state if there is an abundant source of allochthonous sediment during sea level rise. Syvitski et al. (2009) noted that sediment reduction by dam construction can trigger erosion at the delta front. Anthony et al. (2015) observed that dam construction, commercial sand mining and groundwater extraction increased the vulnerability of the Mekong mouth bar area; and that over 300 km of the Mekong delta coastline suffered strong erosion. Dai et al. (2021) noticed that the vegetated mouth bar in the Changjiang Estuary is still present, despite the reduction of fluvial sediment supply caused by the impoundment of the Three Gorges Dam. There is therefore a need to quantify the morphodynamic evolution of deltaic islands and identify the drivers responsible for their

changes. Herein we analyze the variations in deltaic island area in the Atchafalaya River Delta Complex (ARDC) based on a machine learning method applied to the Google Earth Engine cloud computer platform.

The ARDC is a combination of Wax Lake Delta (WLD) and Atchafalaya Delta (AD) in Louisiana. The deltaic islands of both WLD and AD are prograding seaward (Rosen and Xu, 2013). The Atchafalaya River delivers water and sediment from the Mississippi River and Red River into the Gulf of Mexico (Horowitz, 2010). It has formed two sub-deltas through the manmade Wax Lake outlet channel and the natural Atchafalaya River channel since the 1950 s (Shlemon, 1975). After the early 1970s riverine floods, the subaqueous portion of both deltas developed into the WLD and AD (Roberts et al., 1980). Rosen and Xu (2013), using Landsat images at ~ 5-year intervals, found that the deltaic islands of ARDC prograded seaward in recent decades despite a decrease in sediment discharge. Shaw et al. (2014) estimated that the growth rate of the total area of the subaqueous part of WLD was 1.83 km^2/yr between 1974 and 2016. Carle et al. (2015) found a net growth of 6.5 km^2 in the deltaic islands of WLD after the historic flood of 2011 and observed that the vegetation community exhibits a sharp zonation along the island's elevation gradient. Bevington et al. (2017) investigated the relative contribution of river flooding, hurricanes, and cold fronts on elevation change in WLD and suggested that river flood caused the highest deltaic wetland sediment retention. Olliver et al (2020) showed that aerially-averaged vertical accretion in WLD increases from 0.33 to 2 cm in the 60 days when riverine floods are present. Elliton et al. (2020) found that interactions between physical and biophysical processes regulate sediment transport in the deltaic islands of WLD. In summary, previous works have paid considerable attention to the dynamics of WLD (Bevington et al., 2017; Carle et al., 2015; Elliton et al., 2020), but little information is available for the AD. Moreover, some studies observed that hurricanes may cause either degradation by transporting sediment away from deltaic islands, or siltation by delivering coastal sediments (Walker, 2001; Barras, 2007). However, the short-term impact of floods, hurricanes, and other storm events on deltaic islands is difficult to capture by sparse data remote sensing data at ~ 5-year intervals (Rosen and Xu, 2013). Therefore, it is essential to comprehensively understand the ARDC's morphodynamic response to external forcing using high temporal resolution and long-term datasets.

Most studies on the dynamics of deltaic islands were based on field observations (DeLaune et al. 2016; Bevington et al., 2017; Elliton et al., 2020). Hydrodynamic (Nardin et al., 2016; Pertiwi et al., 2021) and morphological models (Fitzgerald, 1998; Roberts et al., 2003) were also introduced to analyze temporal and spatial changes in deltaic islands. However, these methods are time-consuming and laborious, and are difficult to carry out on a large scale to analyze temporal and spatial dynamics of deltaic islands. In recent years, remote sensing images have been used to monitor the morphodynamics of deltaic islands (Rosen and Xu, 2013; Zhang et al., 2021). Google Earth Engine (GEE), a cloud computing platform able to quickly process millions of images (Gorelick et al., 2017; Zhang et al., 2022), has successfully produced annual maps of tidal flats (Wang et al., 2020), forests (Chen et al., 2017), mangroves (Long et al., 2021, 2022) and open water bodies (Zou et al., 2017).

GEE provides many machine learning algorithms that are effectively utilized to extract land use type (Farad, 2017), explore groundwater arsenic distribution (Fu et al., 2022), discern mangrove dynamic processes (Long et al., 2021,2022), and estimate water quality (Guo et al., 2021). Random Forest (RF), a non-parametric machine learning algorithm, has been used to classify spectral characteristics of different landforms. Magidi et al. (2021) applied the RF algorithm to distinguish irrigated and rainfed areas in the Mpumalanga Province in Africa. Long et al. (2021) used the RF algorithm to discriminate tidal flats, mangroves and water bodies in the Nanliu River Delta. Lou et al. (2022) utilized the RF algorithm to classify open water, salt marshes, and mudflats in the Changjiang River Delta. In this study, we aim to explore spatio-temporal dynamics of the deltaic islands in ARDC from 1991 to 2019 using time series of Landsat images and the RF algorithm through the GEE platform.

Table 1
Deltaic island area in the WLD corresponding to tide level at Grand Isle station, Overall accuracy and Kappa coefficient.

Image time	Tide level (m)	Area (km^2)	Overall accuracy	Kappa coefficient
1991-06-20	0.00	21.90	0.957	0.913
1992-09-10	0.35	15.02	0.956	0.963
1993-06-09	0.29	23.48	0.975	0.949
1994-08-15	0.22	22.27	0.967	0.986
1995-09-03	0.18	28.30	0.980	0.961
1996-07-03	0.16	30.67	0.942	0.933
1997-09-08	0.12	27.96	0.985	0.969
1998-07-09	0.18	28.70	0.933	0.942
1999-09-14	0.16	27.88	0.998	0.997
2000-09-16	0.16	29.97	0.965	0.921
2001-09-27	0.17	27.19	0.994	0.987
2002-08-05	0.25	24.06	0.958	0.932
2003-07-07	0.16	25.04	0.974	0.948
2004-07-25	0.14	28.14	0.976	0.925
2005-08-13	0.08	30.72	0.965	0.930
2006-09-01	0.16	24.22	0.992	0.899
2007-09-20	0.13	26.11	0.985	0.969
2008-09-22	0.23	26.59	0.932	0.973
2009-08-24	0.19	25.87	0.939	0.878
2010-09-28	0.09	29.85	0.925	0.913
2011-08-30	0.17	38.00	0.990	0.979
2013-06-16	0.16	37.30	0.943	0.925
2014-09-23	0.32	36.48	0.955	0.965
2015-07-08	0.16	43.68	0.989	0.979
2016-09-28	0.35	34.50	0.980	0.933
2017-09-15	0.20	39.59	0.935	0.912
2018-09-18	0.28	36.85	0.966	0.924
2019-09-05	0.15	38.78	0.985	0.970

The specific objectives are to detect morphodynamic variations of deltaic islands in the ARDC and to diagnose the main drivers that can be responsible for these variations. This study could provide critical insight for the restoration and sustainable management of deltaic islands in the Mississippi River Delta and in other deltas around the world.

2. Materials and methods

2.1. Study area

The Mississippi River is the fourth longest river in the world, starting from the source of the Missouri River, the largest tributary in the Rocky Mountains, with a length of 6262 km. The basin covers an area of 3.23

Table 2
Deltaic island area in the AD corresponding to tide level at Grand Isle station, Overall accuracy and Kappa coefficient.

Image time	Tide level (m)	Area (km^2)	Overall accuracy	Kappa coefficient
1991-06-20	0.00	23.17	0.981	0.962
1992-09-10	0.35	24.88	0.926	0.986
1993-06-09	0.29	30.75	0.953	0.968
1994-08-15	0.22	33.71	0.968	0.988
1995-09-03	0.18	36.22	0.991	0.983
1996-07-03	0.16	41.95	0.986	0.987
1997-09-08	0.12	39.88	0.975	0.988
1998-07-09	0.18	48.25	0.977	0.986
1999-09-14	0.16	41.95	0.991	0.982
2000-09-16	0.16	37.25	0.956	0.976
2001-09-27	0.17	42.91	0.965	0.985
2002-08-05	0.25	35.19	0.958	0.966
2003-07-07	0.16	36.51	0.993	0.987
2004-07-25	0.14	44.63	0.986	0.954
2005-08-13	0.08	46.30	0.976	0.966
2006-09-01	0.16	42.09	0.972	0.986
2007-09-20	0.13	41.35	0.995	0.989
2008-09-22	0.23	38.10	0.983	0.989
2009-08-24	0.19	43.03	0.965	0.978
2010-09-28	0.09	47.74	0.968	0.987
2011-08-30	0.17	49.55	0.994	0.989
2013-06-16	0.16	48.40	0.942	0.986
2014-09-23	0.32	50.39	0.969	0.983
2015-07-08	0.16	51.79	0.992	0.985
2016-09-28	0.35	45.95	0.983	0.985
2017-09-15	0.20	43.22	0.953	0.966
2018-09-18	0.28	48.09	0.965	0.985
2019-09-05	0.15	51.68	0.994	0.987

million km^2, about 1/4 of the area of America (Xu, 2010). Nowadays, the Mississippi River carries a flow of about 380 km^3/yr and transports a sediment load of about 180 million tons to the Gulf of Mexico (Yang et al., 2021). As much as 10,000 to 13000 km^2 of the Mississippi River Delta may be lost or submerged because of SLR and subsidence by 2100 (Olson and Suski, 2021). Given the low wave energy and limited tidal range relative to the river discharge, the Mississippi River Delta is considered a fluvial-dominated system (Keim et al., 2007; Bevington et al., 2017). The Mississippi River Delta was shaped by river flooding, tropical cyclones, and a predominantly east-to-west longshore current (Bevington et al., 2017).

The Atchafalaya River (AR) is the largest tributary of the lower Mississippi River, with a length of about 190 km, and can capture about 30% of the Mississippi River discharge at the Old River Control Structure (ORCS) and the entire flow of the Red River (Horowitz, 2010). This water enters the Gulf of Mexico through the Wax Lake outlet channel and Atchafalaya River main channel, and forms the deltaic islands in the WLD and AD, respectively (Fig. 1A; Horowitz, 2010; Xu and Bryant-mason, 2011). The ORCS was built in 1963 to prevent the avulsion of the Mississippi River into the channel of the Atchafalaya River (Horowitz, 2010). Fluvial water and sediment discharge entering the Gulf of Mexico have obvious seasonal variations, with annual river floods occurring in spring (Mossa and Roberts, 1990). Both WLD and AD encompass several deltaic islands dominated by freshwater plants, such as *Sagittaria, Salix nigra, Typha, Polygonum, Nelumbo, and Phragmites australis* (Rosen and Xu, 2013; Carle et al., 2015). According to different hydrological connectivity with the surrounding distributary channels (Olliver and Edmonds, 2021), the deltaic islands of WLD could be divided into three parts: the western part (WP), the central part (CP), and the eastern part (EP) with their own distinct regional deposition features and different sediment transport regimes, same for the AD (Fig. 1C-D).

2.2. Materials

In this study, a total of 262 remote sensing images from Landsat 5 TM (1991–2011), Landsat 7 ETM (2002–2003) and Landsat 8 OLI (2011–2019) are used to analyze the morphodynamic variations of the deltaic islands in the ARDC (United States Geological Survey, USGS, https://earthexplorer.usgs.gov). Yearly tide level data from 1991 to 2019 at Grand Isle station and USGS Atchafalaya 2 Lidar data were downloaded from the National Oceanic and Atmospheric Administration (NOAA) (https://www. noaa.gov). Landsat images from June to September at similar low water level at Grand Isle were selected to minimize the impact of tidal levels and seasons on the delta evolution analysis (Table 1, 2). Daily mean water discharge and annual suspended sediment discharge (SSD) at Wax Lake Outlet near Calumet (WLO) and Morgan City, Louisiana (MC) were collected from USGS (https://waterdata.usgs.gov/nwis). These data record the water flow and SSD through the Wax Lake outlet channel and Atchafalaya River main channel from 1991 to 2019. The annual water discharge for each year is counted by the sum of daily discharge within a year. In addition, information about hurricanes and storm events occurring within 500 km from the ARDC was collected from NOAA in the period 1991–2019 (Table 3). The surface elevation measured with Rod Surface Elevation Tables at the CRMS0479 in the WLD for the period of 19 February 2009—8 March 2021 and at the CRMS6304 in the AD for the period of 19 October 2009–28 January 2021 were collected from the Coastwide Reference Monitoring System (https://www.lacoast.gov/crms/).

2.3. Methods

2.3.1. Methodological framework

We classified deltaic islands and open water in the ARDC through a machine learning algorithm based on the GEE platform (Fig. 2A; Lou et al., 2022). The procedure to classify deltaic islands and open water followed four steps: (1) training samples, (2) feature extraction, (3) separating deltaic island from open water using spectral indices, and (4) vectorization and edge lines extraction (Fig. 2A). Note that the white land that appeared suddenly on the Landsat images and that is distinctly different from the surrounding vegetated deltaic land and seawater was recognized as dredged spoil (Zhang et al., 2021). These white zones were outlined manually for further analysis.

2.3.1.1. Training and validation samples. In order to investigate the evolution of the deltaic islands, we divided the ARDC into two categories - deltaic island and open water - through visual interpretation of high-resolution images from Google Earth. Firstly, two layers were constructed and a class label (deltaic islands and open water) was assigned

Table 3
Hurricane and storm events that have impacted the ARDC during 1991–2019 and the corresponding area changes.

Name	Year	Category	Distance (km)	Direction	Max wind speed (km/h)	Area change of the WLD (km^2)	Area change of the AD (km^2)
Andrew	1992	3	20	W	185.2	−3.86	1.56
Opal	1995	3	408	E	203.72	−2.35	−5.36
Josephine	1996	TS	184	E	111.12	−2.02	2.72
Danny	1997	1	85	E	129.64	0.35	2.54
Georges	1998	2	286	E	166.68	−2.33	0.23
Allison	2001	TS	19	W	92.6	−3.46	−0.96
Isidore	2002	TS	120	E	101.86		
Lili	2002	1	63	W	148.16	−5.34	−6.98
Matthew	2004	TS	70	E	74.08	0.43	2.23
Katrina	2005	3	180	E	203.72	−4.88	−3.11
Rita	2005	3	120	W	185.2	2.33	−0.28
Humberto	2007	1	246	W	148.16	−0.76	−1.01
Gustav	2008	2	70	E	166.68	−1.78	−6.56
Ike	2008	2	324	W	175.94		
Isaac	2012	TS	134	E	111.12		
Cindy	2017	TS	218	E	83.34	−8.47	2.89
Harvey	2017	TS	205	W	74.08	−6.08	−0.50
Nate	2017	1	218	E	138.9	3.50	−2.63
Gordon	2018	TS	200	E	111.12	−3.96	−0.80
Barry	2019	1	75	W	120.38	−5.38	0.81

*Category is the Saffir-Simpson scale and identifies the wind strength of the storm at landfall. TS = Tropical storm, 63–118 km h^{-1}; category 1 = 119–153 km h^{-1}; category 2 = 154–177 km h^{-1}, Category 3 = 178–208 km h^{-1} (Rosen and Xu, 2013). Distance refers to the distance of hurricane and tropical storm from the ARDC center (Fig. 1).

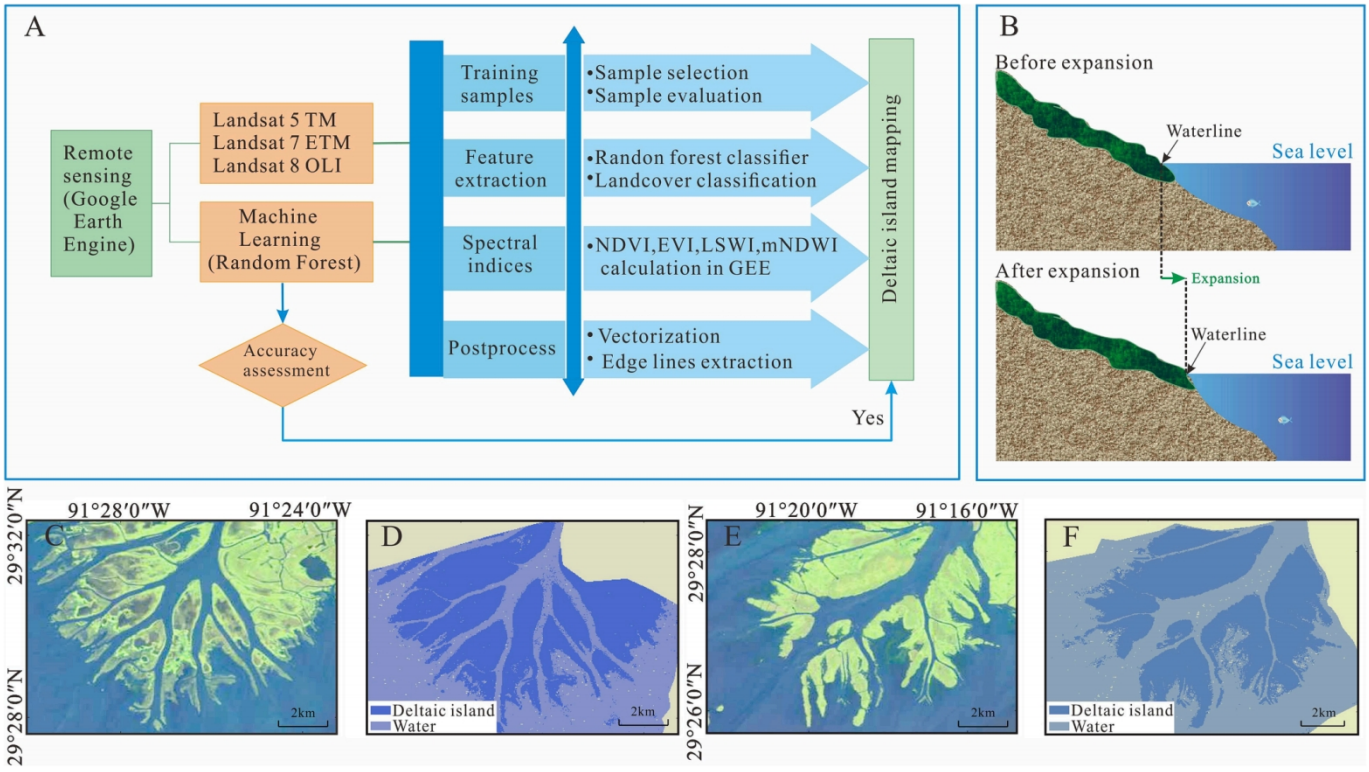

Fig. 2. Image processing workflow and schematic maps of deltaic island and water bodies. A. The workflow of the images processing; B. The determination of waterline. C. Landsat image of WLD; D. Map of deltaic islands and water in WLD distinguished by the RF algorithm; E. Landsat image of AD; F. Map of deltaic island and water in AD distinguished by the RF algorithm.

to each layer; then, dozens of training polygons were manually selected and 1500 random points were generated by the 'random Point' command in GEE. Among them, 70% were set as training samples and the remaining 30% were set as validation samples.

2.3.1.2. Spectral indices calculation. The pixel-based supervised RF algorithm effectively classify spectral characteristics of different landforms and discriminate deltaic islands from open water according to four spectral indices: Normalized Difference Vegetation Index (NDVI) (Rouse et al., 1974), Enhanced Vegetation Index (EVI) (Huete et al., 2002), Land Surface Water Index (LSWI) (Xiao et al., 2004) and modified Normalized Difference Water Index (mNDWI) (Xu, 2006):

$$NDVI = \frac{\rho_{NIR} - \rho_{RED}}{\rho_{NIR} + \rho_{RED}} \quad (1)$$

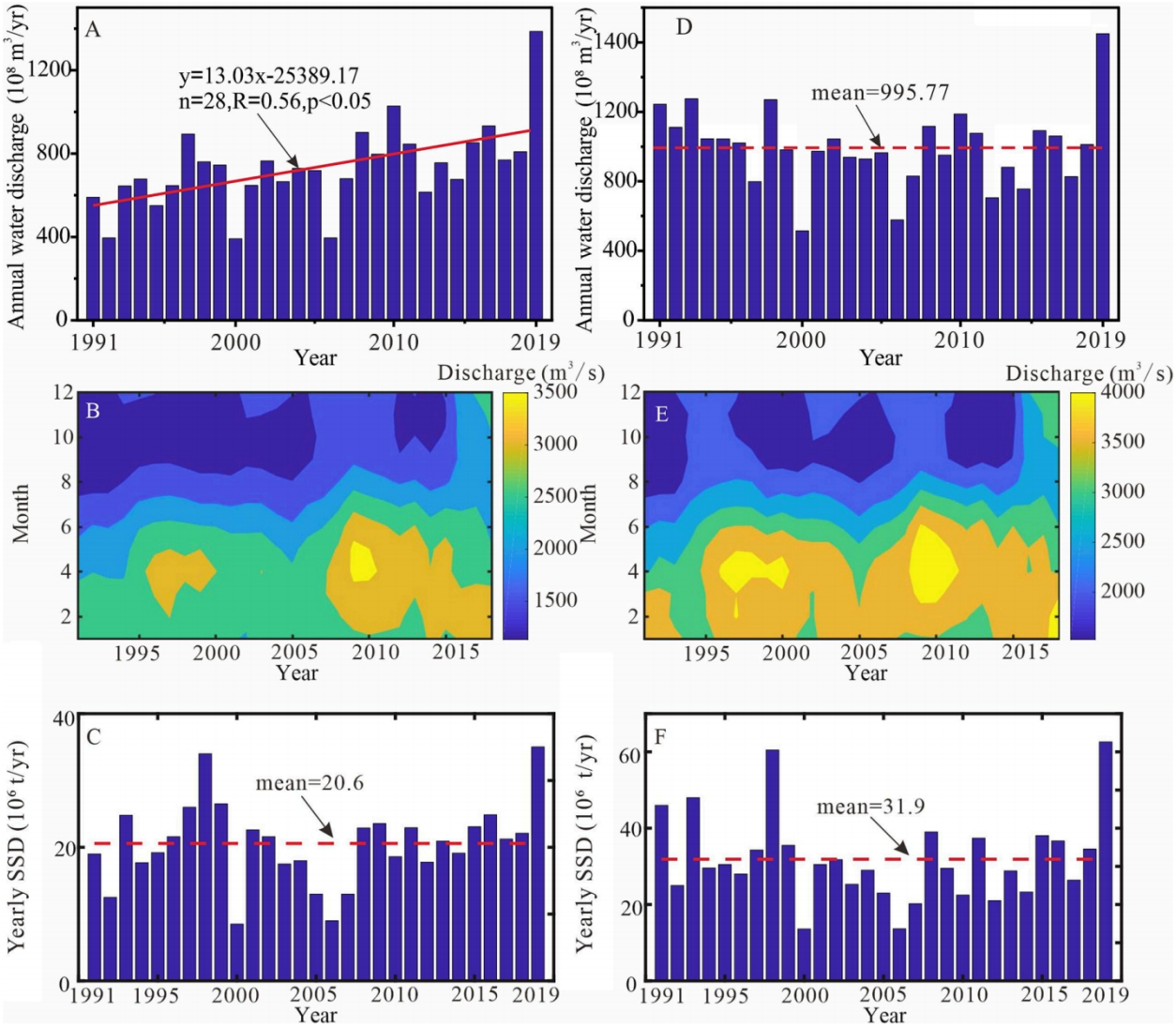

Fig. 3. Changes in water discharge and SSD. A. Annual water discharge at WLO; B. Monthly water discharge at WLO; C. Yearly SSD at WLO; D. Annual water discharge at MC; E. Monthly water discharge at MC; F. Yearly SSD at MC.

$$EVI = 2.5 \times \frac{\rho_{NIR} - \rho_{RED}}{\rho_{NIR} + 6\rho_{RED} - 7\rho_{BLUE} + 1} \quad (2)$$

$$LSWI = \frac{\rho_{NIR} - \rho_{SWIR}}{\rho_{NIR} + \rho_{SWIR}} \quad (3)$$

$$mNDWI = \frac{\rho_{GREEN} - \rho_{SWIR}}{\rho_{GREEN} + \rho_{SWIR}} \quad (4)$$

Where ρ_{BLUE}, ρ_{GREEN}, ρ_{RED}, ρ_{NIR}, ρ_{SWIR} are the blue, green, red, near-infrared, and shortwave infrared bands of Landsat images, respectively. The value of these spectral indices was extracted for each pixel in the training dataset.

2.3.1.3. Random forest classification. RF classifier uses a set of decision trees to predict classification or regression with the advantages of high precision, efficiency, and stability (Belgiu and Dragut, 2016). This ensemble classifier has been widely used in remote sensing data for land cover classification (Lou et al., 2022; Bwangoy et al., 2010). GEE has programmed the RF algorithm on their API to be used to classify available satellite images. Here, "ee.Classifier.randomForest" function within the GEE platform was utilized for training a random forest classifier, using the extracted spectral indices and their corresponding class labels as input datasets. Ultimately, the entire image was classified by utilizing the trained random forest classifier, which was applied to the spectral index values, resulting in the production of a classification map.

2.3.1.4. Accuracy assessment. Error analysis is necessary to verify the accuracy of the remote sensing resolution and images processing (Lawrence and Wright, 2001). For a better interpretation and correct identification of features, the minimum level of accuracy of a classified map should be over 85% (Kumar et al., 2021). The accuracy assessment generally includes an error matrix, user accuracy, producer accuracy, overall accuracy, and kappa coefficient (Kumar et al., 2021). Here, the overall accuracy ranged between 0.925 and 0.998, kappa coefficients for all observation years were higher than 0.899, and met the minimum analysis requirements, deeming the classification accuracy as acceptable (Table 1, 2).

2.3.1.5. Postprocessing. The post-processing of Landsat images included images vectorization, area calculation and waterlines extraction. The images vectorization transformed the classification map into a vector map using the "ee.Image.reduceToVectors" function. Then "pixelArea" in GEE was used to calculated the area of deltaic islands. The waterline is the interface between water body and deltaic island, which is the dry-wet boundary (Geleynse et al., 2015). The waterline on the islands is

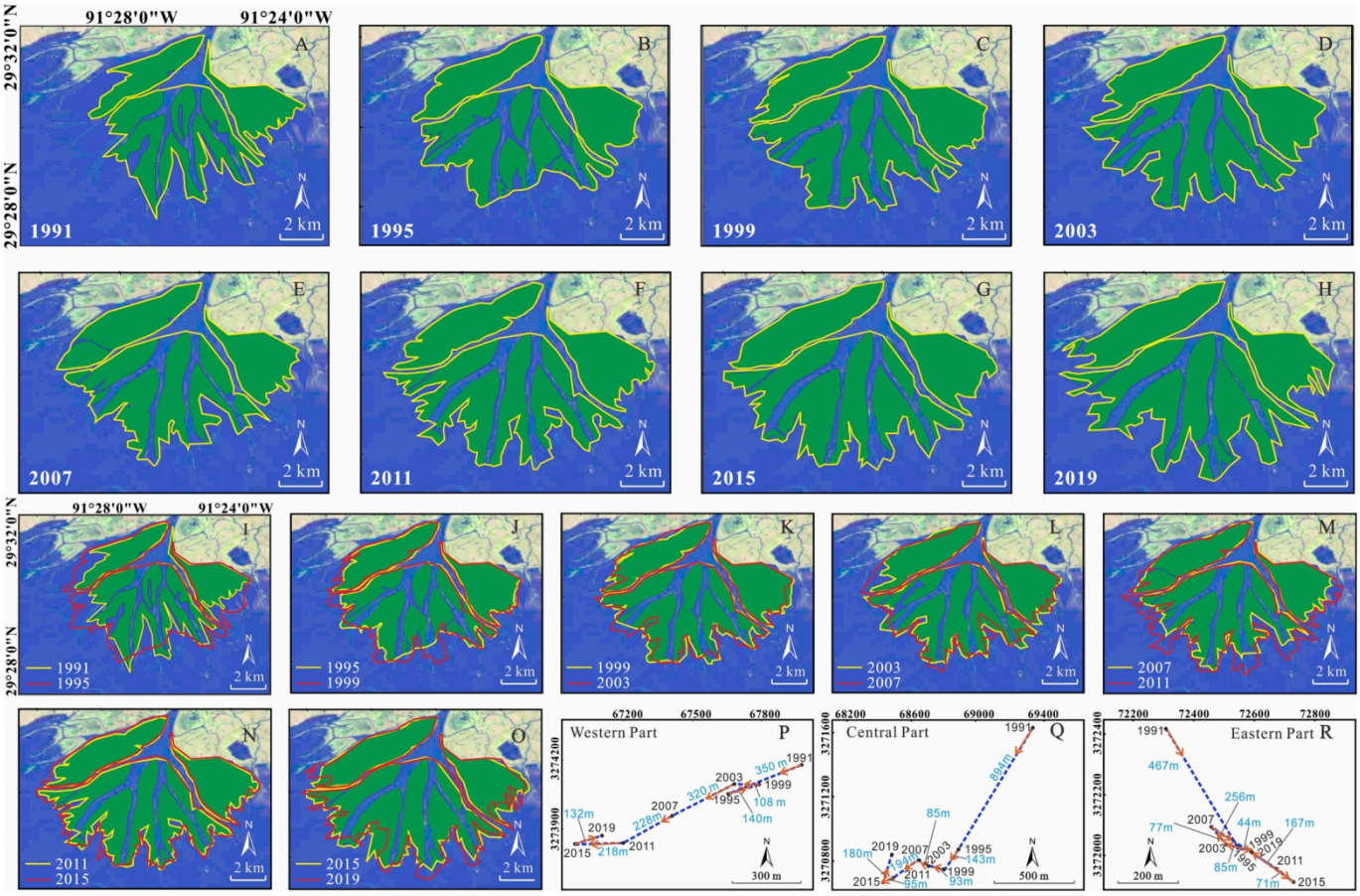

Fig. 4. Morphological changes of deltaic islands in WLD between 1991 and 2019. P-R. Migration of center of mass of WP, CP and EP.

automatically classified by the RF, while the manual extraction is needed to connect the islands and create a uniform shoreline. For a fixed tidal level, waterlines expanding seaward suggests that the deltaic islands are prograding (Fig. 2B).

2.3.2. Center of mass of deltaic islands

The center of mass model is widely applied to detect variations in population distribution, trends in regional economic growth, land use, and distribution and ecological parameters (Na et al., 2019; Guo et al., 2020; Meng et al., 2021). This study uses the center of mass model to calculate the center of mass coordinates of the deltaic islands, and to analyze their change from 1990 to 2019. The equations of the center of mass are as follows:

$$\bar{X}_i = \frac{\sum_{i=1}^{n} X_i A_i}{\sum_{i=1}^{n} A_i} \tag{5}$$

$$\bar{Y}_i = \frac{\sum_{i=1}^{n} Y_i A_i}{\sum_{i=1}^{n} A_i} \tag{6}$$

Where:$\bar{X}_i$,$\bar{Y}_i$ refer to the center of mass coordinates; X_i, Y_i are the longitude and latitude coordinates of the ith pixel; and A_i is the area of the ith pixel.

2.3.3. Rod surface elevation table

In the CRMS network, the Rod Surface Elevation Table (RSET) method is used to estimate surface elevation change rates. One RSET benchmark is located at each CRMS site. From the RSET benchmark, surface elevation is measured at nine points in four directions to calculate elevation change at 6-month intervals. Specifically, the benchmark time is 2009/10/19 at the CRMS6304 in the WLD and 2009/2/19 at the CRMS0479 in the AD. In the CRMS, surface elevation change is defined as cumulative elevation change since station establishment. For each sampling event, mean cumulative elevation change is calculated for each of the four directions, and an elevation change rate is estimated using linear regression of elevation change against time.

In addition, we constructed DEM using lidar data of the subaerial islands collected during the USGS Atchafalaya 2 Lidar campaign (NOAA, 2011). Transects were selected about 200 m interval for each delta, extending 1 km from the shoreline in 2019 landwards (Fig. S1). We have calculated the slope (S) of selected transects, and then calculated the vertical deposition rate (V, mm/yr) based on the slope and shoreline expansion rate (R, m/yr), according to the following formula:

$$S = \frac{\Delta Z}{\Delta L} \tag{7}$$

$$V = S^{*}R/1000 \tag{8}$$

Where: ΔZ is height difference between the start and end of the transect (m); ΔL is distance between the start and end of the transect (m). The results are shown in Table 3.

3. Results

3.1. Variations in water discharge and SSD

The water discharge and SSD delivered into the ARDC at WLO and MC presented different oscillations between 1991 and 2019 (Fig. 3). Specifically, the water discharge at WLO station exhibited a significantly upward trend (Fig. 3A). The monthly water discharge displayed a seasonal variation with a flood season between January and June and a dry season from July to December (Fig. 3B). The mean water discharge of

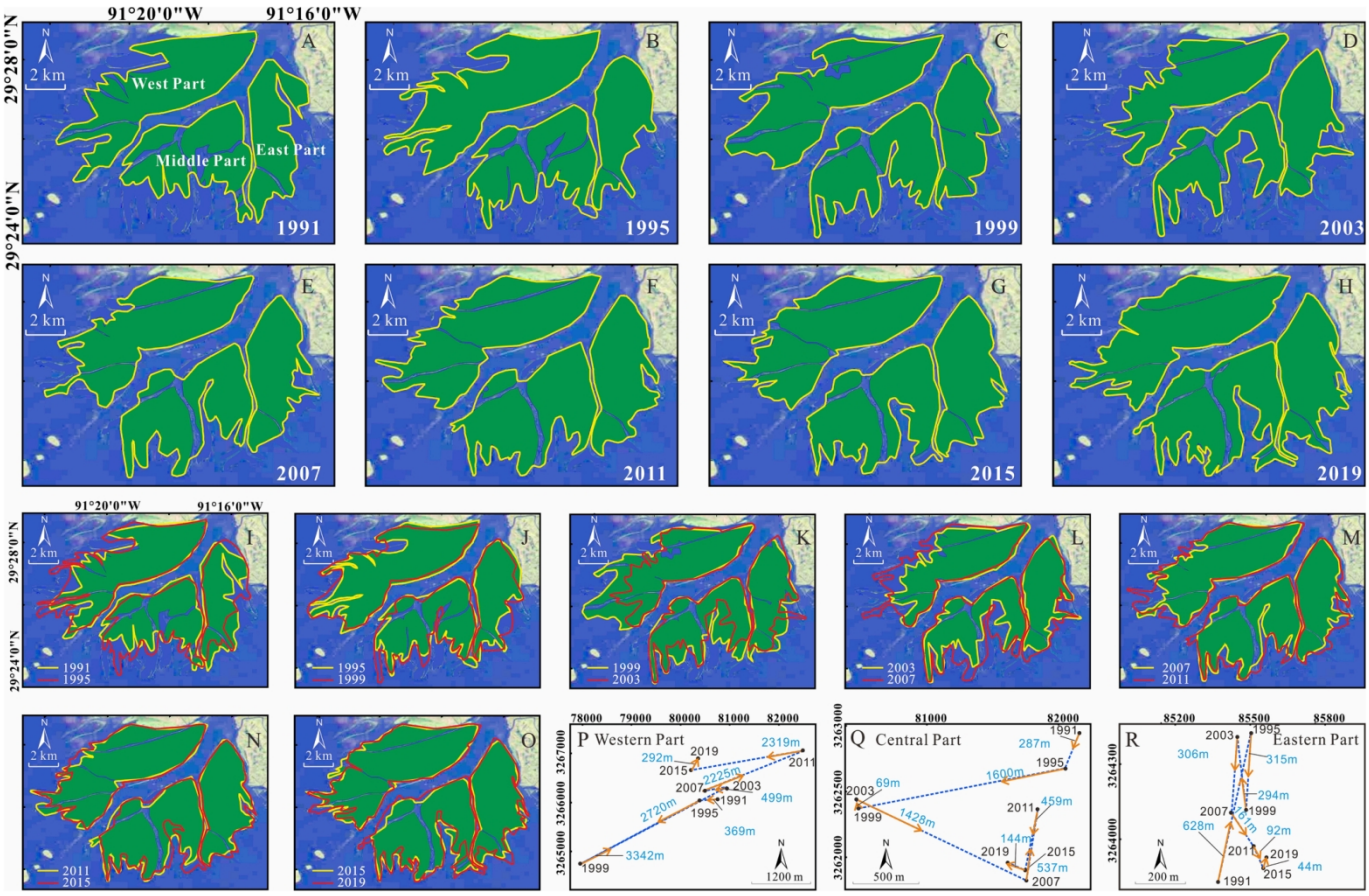

Fig. 5. Morphological changes of deltaic islands in AD between 1991 and 2019. P-R. Migration of center of mass of WP, CP and EP.

the flood and dry seasons was 2971 m^3/s and 1662 m^3/s, respectively. In addition, the annual SSD ranged from 0.85 × 10^7 t to 3.50 × 10^7 t between 1991 and 2019, with an average value of 2.06 × 10^7 t (Fig. 3C).

The records of the MC station indicate that the yearly water discharge changed little between 1991 and 2019, fluctuating around 995.77 × 10^8 m^3/yr (Fig. 3D). The monthly water discharge displayed seasonal variations, with the mean water discharge during the flood and dry seasons equal to 3751 m^3/s and 2164 m^3/s, respectively (Fig. 3E). Furthermore, the mean yearly SSD ranged from 1.36 × 10^7 t to 6.26 × 10^7 t during 1991–2019, with a mean value of 3.19 × 10^7t (Fig. 3F).

3.2. Migration of center of mass of deltaic islands

The shape of WLD has little changed from 1991 to 2019, only the seaward waterline presented progradation or recession (Fig. 4). The WP of the WLD was basically unchanged from 1991 to 2019. The waterline of the WP remained relatively smooth with little change at the water edge, except for some indentations in the distal part of the islands. In the same period, the waterline of the WP moved 780 m southwestward in the bay with an average rate of 26 m/yr, and the expansion rate ranged between −36 m/yr and 60 m/yr. The center of mass of WP migrated approximately 766 m southwest from 1991 to 2019 (Fig. 4P). The center of mass initially moved southwest by 350 m between 1991 and 1995, but then shifted northeast by 140 m from 1995 to 1999. It moved southwest again by 320 m between 2003 and 2007, followed by a westward shift of 228 m from 2011 to 2015, and finally northeast by 132 m from 2015 to 2019. The configuration of the CP of the WLD was characterized by several distributary channels and related mouth bars forming deltaic islands. During 1991–2019, the islands expanded southward with an average rate of 45 m/yr. The expansion rate was approximately 125 m/yr from 1991 to 1995, and then slowed down and remained almost stable around 20 m/yr after 1999. The center of mass of CP migrated from northeast to the southwest approximately 1175 m from 1991 to 2019 (Fig. 4Q). Note that the center of mass changed significantly between 1991 and 1995, presenting a southwest movement of 894 m, which is followed by a slower migration, 143 m southwest, between 1995 and 1999. The center of mass moved northwest approximately 93 m and 85 m in the period of 1999–2003 and 2003–2007, respectively. The center of mass then shifted southwest about 194 m and 95 m in the period of 2007–2011 and 2011–2015. During 2015–2019, the center of mass shifted about 180 m northeast. The EP waterline moved seawards 580 m over the period between 1991 and 2019 with an average rate of 19 m/yr. The maximum expansion rate of the waterline was 114 m/yr during 1991–1995 and then receded by 6 m/yr from 1999 to 2003 (Fig. 4K). The center of mass of the EP moved southeastward about 500 m during the period from 1991 to 2019 (Fig. 4R). A major migration occurred between 1991 and 1995, when the center of mass exhibited a southeast movement of about 467 m, which then shifted about 154 m northwest from 1999 to 2007. During 2007–2019, the center of mass generally migrated southeast, though there was a 167 m northeastwards migration between 2015 and 2019.

In AD, the waterline of WP expanded 750 m seaward from 1991 to 2019 (Fig. 5). In particular, the waterline suggested a retreat rate of 24 m/yr from 1999 to 2003 followed by a fast expansion of 30 m/yr during 2003–2007 (Fig. 5K, L). The waterline migration slowed down and remained relatively stable with an expansion rate of only 3 m/yr after 2007 (Fig. 5M–O). The center of mass of WP exhibited a series of dramatic shifts during 1995–2019, namely, a 2720 m southwest movement from 1995 to 1999, a 3342 m northeast migration in the period of 1999–2003, a further 2225 m northeast migration during 2007–2011, a 2319 m southwest shift from 2011 to 2015 and then a 292 m northeast movement in the period 2015–2019 (Fig. 5P). The waterline of CP

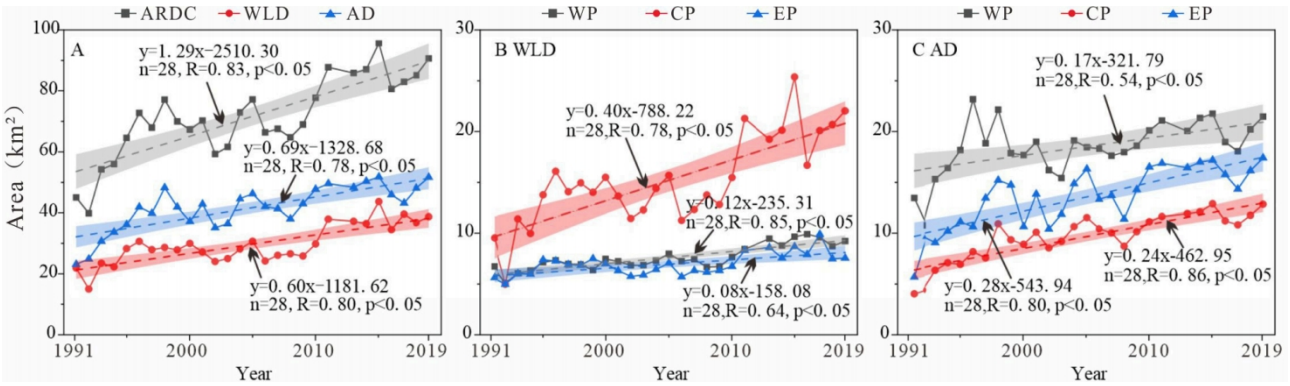

Fig. 6. Temporal changes in deltaic island area.

moved 1300 m seawards from 1991 to 2019 with an expansion rate of 43 m/yr. The maximum expansion rate was 100 m/yr from 1991 to 1995, but a recession occurred in the period 1999–2003 (Fig. 5I, K). The center of mass of CP moved approximately 287 m southwestward between 1991 and 1995, which was followed by a 1600 m southwest migration between 1995 and 1999 and a significant 1428 m southeast migration from 2003 to 2007. After 2007, the center of mass shifted to the northwest (Fig. 5Q). The waterline of EP remained basically stable, moving 30 m seaward over the period 1991–2019 (Fig. 5I-K). The center of mass presented a southeastward migration by approximately 219 m over the period 1991–2019 (Fig. 5R), with a notable northeast migration been detected between 1991 and 1995, when the center moved about 628 m. In the following periods of 1995–1999 and 2003–2007, the center of mass migrated southwest successively by 315 m and 306 m, and then shifted about 224 m southeast during 2007–2019.

3.3. Areal change of deltaic islands

The total area of deltaic islands in ARDC linearly increased from 45.07 km^2 in 1991 to 90.46 km^2 in 2019, indicating an annual increasing trend of 1.29 km^2/yr over the past 30 years ($p < 0.05$, Fig. 6A). However, the change of islands area in different regions of the ARDC displays some variability.

In the WLD, the deltaic islands increase from 21.90 km^2 in 1991 to 38.78 km^2 in 2019, with a linear rate of 0.60 km^2/yr ($p < 0.05$, Fig. 6A). The area in the WP and EP increased with a constant rate of 0.12 km^2/yr and 0.08 km^2/yr in the period of 1991 to 2019 (Fig. 6B); while the area of CP gained about 12.45 km^2, with a mean rate of 0.40 km^2/yr (Fig. 6B). In the AD, the islands area increased from 23.17 km^2 in 1991 to 51.68 km^2 in 2019, with an increasing rate of 0.69 km^2/yr (Fig. 6A). The deltaic islands in the WP, CP and EP increased at rates of 0.17 km^2/yr, 0.28 km^2/yr and 0.24 km^2/yr, respectively (Fig. 6C).

4. Discussion

Shape and growth of deltaic islands in low-relief alluvial deltas are primarily impacted by riverine flow, sediment supply, waves, human modifications and relative SLR (Fagherazzi et al., 2020; Nardin et al., 2016; Zhang et al., 2021; Carle et al., 2015). In this section, the potential processes controlling variations in deltaic islands area and shape in ARDC are discussed.

4.1. Effect of water discharge and sediment supply

The growth of a river-dominated delta is highly controlled by fluvial sediment and water flow (Lamb et al., 2012; Xu et al., 2021; Dai et al., 2018). The riverine sediments delivered into the delta could deposit on the deltaic islands due to the slowing down of water flow caused by mouth bars and vegetation, both favoring delta formation (Long et al., 2021; Lou et al., 2022). Previous studies observed that coarse sediments

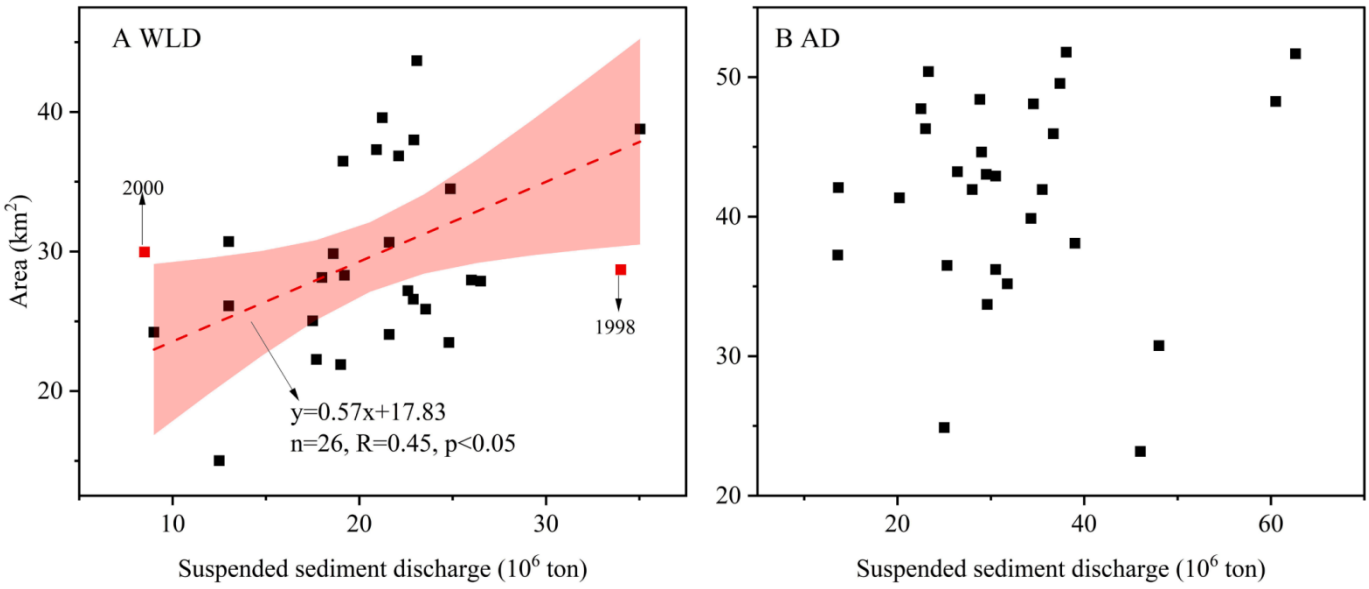

Fig. 7. The relation of SSD and deltaic island area.

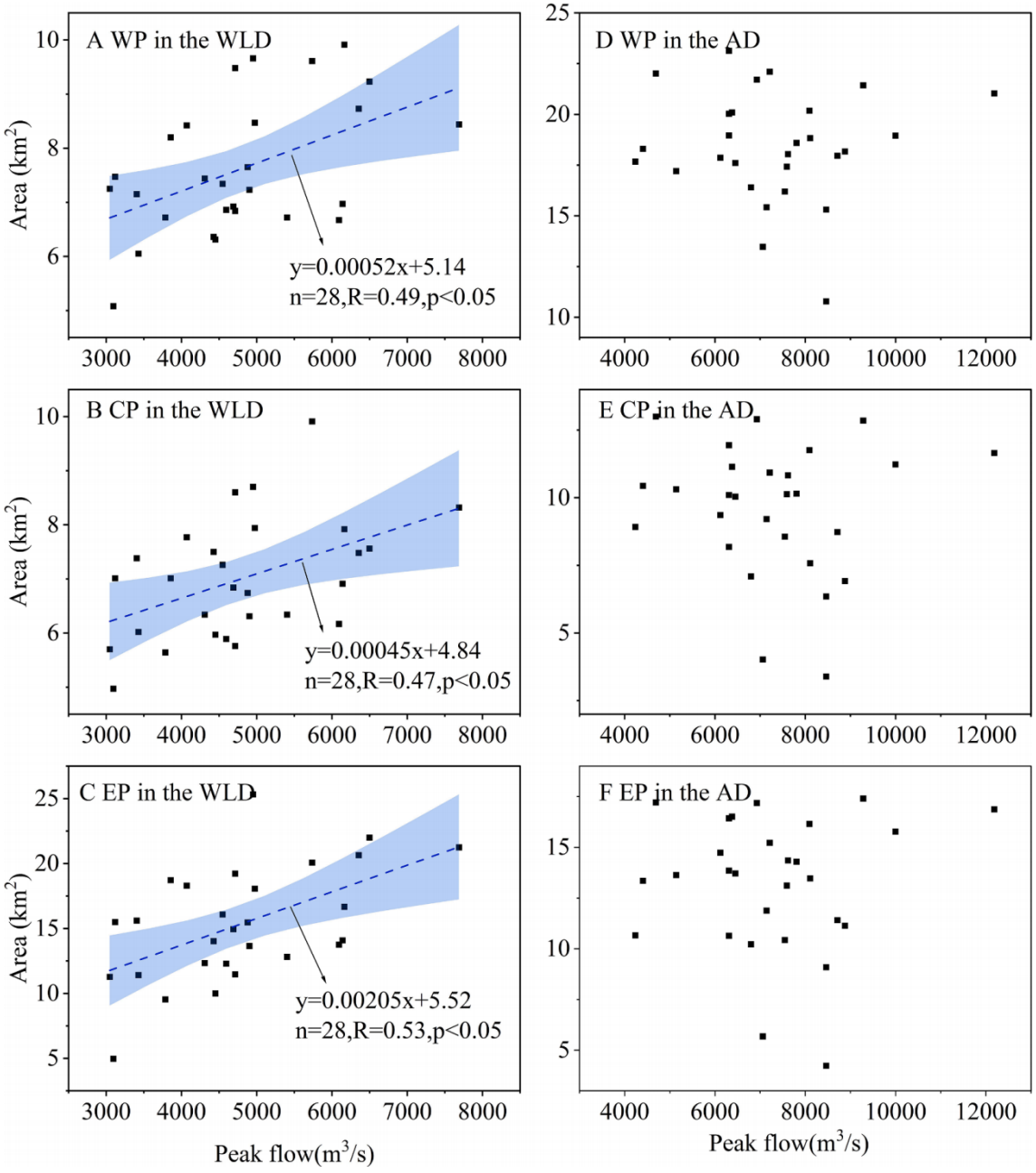

Fig. 8. The relation between peak discharge and deltaic island area of each part.

were important for delta growth, because they overlay fine sediment to create a substrate elevated enough for colonization of marsh plants (van Heerden and Roberts, 1988). Fig. 7A-B describes the relationship between SSD and islands area over the period 1991–2019. Fluvial SSD has positive relation with deltaic island area at a significant level of 0.05 in WLD, meaning that annual riverine suspended sediments have effectively promoted the growth of the delta (Fig. 7A). However, there is no correlation between SSD and deltaic islands area on the AD (Fig. 7B). The Atchafalaya River main channel has experienced aggradation in 1977–2006 between the MC and AD by trapping a considerable volume of riverine sediments (Tang et al., 2021), which significantly reduced the number of sediments entering the delta. In such context, fluvial sediments can no longer support the formation of new land in AD. Other processes are therefore responsible for the growth of the AD islands. This is further discussed in the following section.

Large floods deliver a disproportionate amount of sediment to the coast, and play a critical role in the creation and maintenance of deltas and associated deltaic islands (Nittrouer et al., 2008, 2011; Carle et al., 2015). Nittrouer et al. (2008) found that high discharge events were important for the delivering of coarse sediments (e.g. sand) in the lower Mississippi River, where the bedform transport rate has a positive exponential relationship with discharge. In river-dominated deltas, big floods lead to significant sediment deposition in the delta and on the islands (Carle et al., 2015; Bevington et al., 2017; Oliver et al., 2020). In WLD, peak discharge was positively correlated with the growth of each section of the deltaic islands (Fig. 8A-C), indicating that the expansion of the islands is mainly determined by flood events. During floods, high riverine discharge mobilizes sediments that were deposited in river channels in low-flow conditions and spreads the material over a large area of the deltaic islands (Nittrouer et al., 2011, 2012; Rosen and Xu, 2013). On the contrary, Fig. 8D-F demonstrates that the islands area of the three sub-sections of AD is unrelated to the peak discharge,

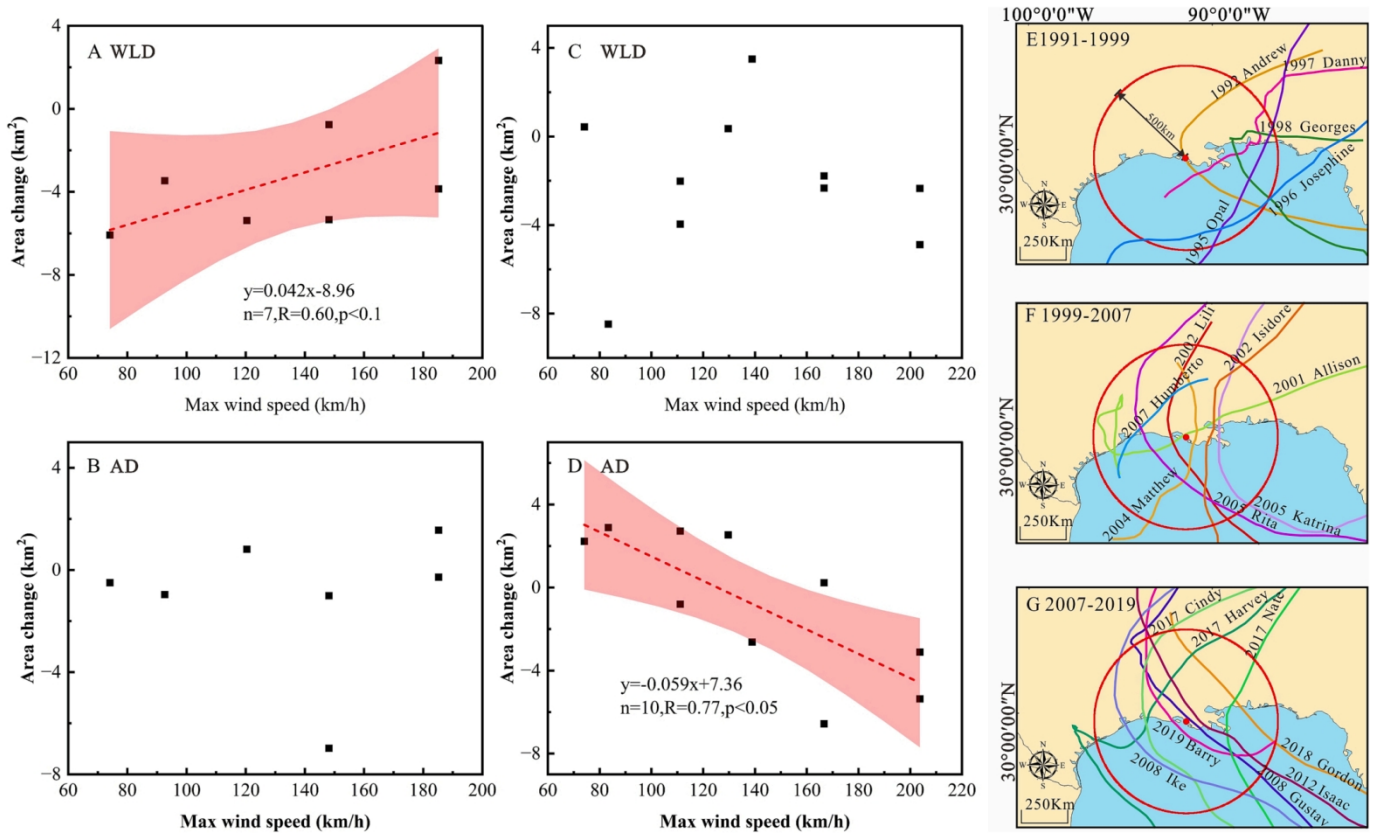

Fig. 9. The relation between max storm wind speed of a tropical cyclone and area changes of deltaic islands. A-B. The relation between max storm wind speed of a tropical cyclone landing west of the ARDC and area change of deltaic islands in WLD and AD; C-D. The relation between max storm wind speed of a tropical cyclone landing east of the ARDC and area change of deltaic islands in WLD and AD; E-G. Hurricane and tropical storm tracks in 1991–1999, 1999–2007 and 2007–2019.

indicating that fluvial flood has no significant effect on the growth of deltaic islands in this delta.

4.2. *Impact of hurricanes and storms*

Hurricanes and storms can erode large parts of deltaic islands (Barras, 2007; Howes et al., 2010) or supply sediment for them (Nyman et al., 1995; Turner et al., 2006; Rosen and Xu, 2013). During 1991–2019, 12 hurricanes and 8 tropical storms landed near the ARDC (Table 3; Fig. 9E-G). In this study, we selected two images at similar tidal level before and after the landfall of hurricanes and tropical storms to quantify the storm effect on the islands (the interval between the two images is about a month). To quantify the effects of hurricanes and tropical storms, we calculated the area generated by fluvial sediments before and after the hurricanes using a positive correlation between SSD and deltaic island area. Then the area difference between the two images before and after each hurricane was used to determine the storm impact on the deltaic islands.

Guntenspergen et al. (1995) observed that Hurricane Andrew, which made landfall 20 km to the west of the ARDC, added on average 16 cm of sediments to the marshes surrounding Atchafalaya Bay. Barras (2003) found that hurricane Lili caused 7 km^2 of marsh loss ~ 21 km west of WLD (Rosen and Xu, 2013). Barras (2007) stated that much of the submerged and floating vegetation in the ARDC was removed by hurricane Rita, a category 3 hurricane with maximum wind speed of 185.2 km/h that made landfall 120 km to the west of WLD in 2005 and eroded more than 500000 m^3 of sediments (Xing et al., 2017). Using two adjacent images before and after the landfall of tropical storm Isidore and Hurricane Lili in 2002, we calculated that the deltaic island in the WLD and AD lost 5.34 and 6.98 km^2, respectively. In summary, hurricanes and tropical storms had a variable impact on both deltas.

Moreover, our data suggest that hurricanes and tropical storms triggered on average erosion in the WLD (Table 3). In particular, the deltaic island areal change has a positive correlation with the maximum wind speed of hurricanes that made landfall western of the deltas at a significance level of 0.1, but there is no correlation between islands areal change and the maximum wind speed of storms that landed eastward of the delta (Fig. 9A, B). On the contrary, hurricanes and tropical storms with different categories and directions caused both short-term deltaic island erosion and progradation in the AD. Specifically, we found a significant negative correlation between the maximum wind speed of a tropical cyclone that landed east to the ARDC and deltaic island erosion (Fig. 9D). However, the same relationship does not hold for hurricanes landing to the west of the delta (Fig. 9C), despite they trigger higher waves and storm surges.

Moreover, saltwater intrusion induced by storm surges could kill most freshwater plants such as *Nelumbo. lutea*, *Sagittaria*, and *Potamogeton. nodosus*, which dominated at the lower elevation on the WLD and AD (Carle et al., 2015; Carle and Sasser, 2016). However, the high freshwater flows from Atchafalaya River upstream flushed salt from soil quickly, preventing long-term increases in pore water salinity in the delta, thus the plants were less affected by saltwater intrusion (Carle and Sasser, 2016). Furthermore, strong winds could cause defoliation and even plant death with much lower spectral reflectance near infrared (700–1300 nm), consequently lead to lower NDVI values (<0.2), indicating that the defoliation and dead vegetation may not be extracted from GEE (Li and Guo, 2010; Carle and Sasser, 2016). Therefore, the effects of hurricane induced defoliation can be neglected while the effect of hurricane caused plant death is considered as the unrecognized dead vegetation area in this study.

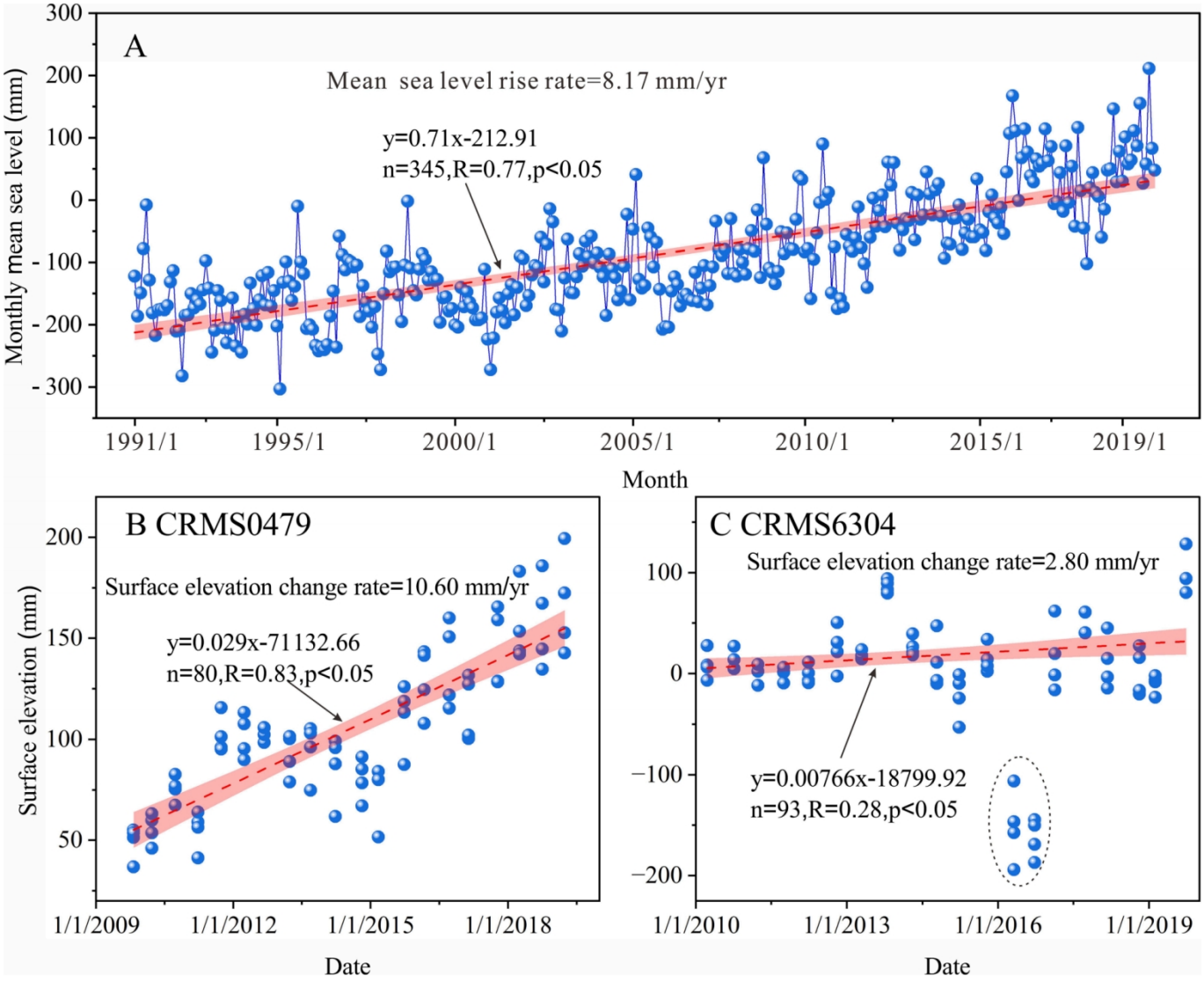

Fig. 10. Sea level rise and deltaic island elevation change. A. Annual mean sea levels at the Grand Isle tidal station between 1991 and 2019; B. Surface elevation change measured at the CRMS0479 in the WLD; C. Surface elevation change measured at the CRMS6304 in the AD. The elevation of highlighted cluster in 2016 was significantly lower compared to the surrounding years, suggesting that these may be anomalous data, and they were excluded to prevent them from influencing the results of the correlation analysis.

Table 4
Slope and vertical deposition rate.

Delta	Regine	Transect	Slope	Expansion rate (m/yr)	Vertical deposition rate (mm/yr)
WLD	WP	1–12	0.00041920	26.00	10.90
	CP	15–36	0.00034802	45.00	15.66
	EP	38–51	0.00057541	19.00	10.93
AD	WP	1–25	0.00093100	25.00	23.28
	CP	28–47	0.00081748	43.00	35.15
	EP	48–66	0.00065490	1.00	0.65

4.3. Sea level rise

Increasing sea levels can severely threaten deltaic islands if their platforms cannot accrete at the same rate (Kirwan et al., 2013; Jankowski et al., 2017; Yang et al., 2021). Global mean SLR has increased by about 8 cm since 1993 (at a rate of 3.0 ± 0.4 mm/yr), because of global warming (Sweet et al., 2017). SLR might exceed 2 m in many regions such as in the contiguous United States by 2100 (Kopp et al., 2017; Lou et al., 2022). At the Grand Isle tidal station, mean sea level has risen at a rate of 8.17 mm/yr since 1991 (Fig. 10 A), three times higher global SLR, due to subsidence. A geodetic study has reported a present-day subsidence rate of 5–10 mm/yr in much of the coastal area of Louisiana and Mississippi (Torbjörn et al., 2006). During our study period, surface elevation measured with RSET has increased by 10.60 mm/yr and 2.80 mm/yr at the CRMS0479 in the WLD and CRMS6304 in AD (Fig. 10B, C). Assuming that the deltas prograde in the gulf with a constant slope, the vertical deposition rates of WP, CP, and EP in WLD should be 10.90 mm/yr, 15.66 mm/yr, and 10.93 mm/yr (Table 4). With a shoreline prograding rate of 25.00 m/yr, 43.00 m/yr, and 1.00 m/yr, the WP, CP, and EP in AD should vertically accrete of 23.28 mm, 35.15 mm, and 0.65 mm per year, respectively to maintain the same topographic slopes. Results suggest that the rate of vertical accretion exceeds SLR, indicating that the delta is not currently facing the threat of inundation, except for the EP of AD (Table 4), which is consistent with the fact that the soil surface accretion rate measured at the CRMS6304 on the EP of the AD is less than SLR (Fig. 10 C).

Note that Wagner et al. (2017) demonstrated that the elevation of WLD has increase and slope tended to slow down. Therefore, assuming

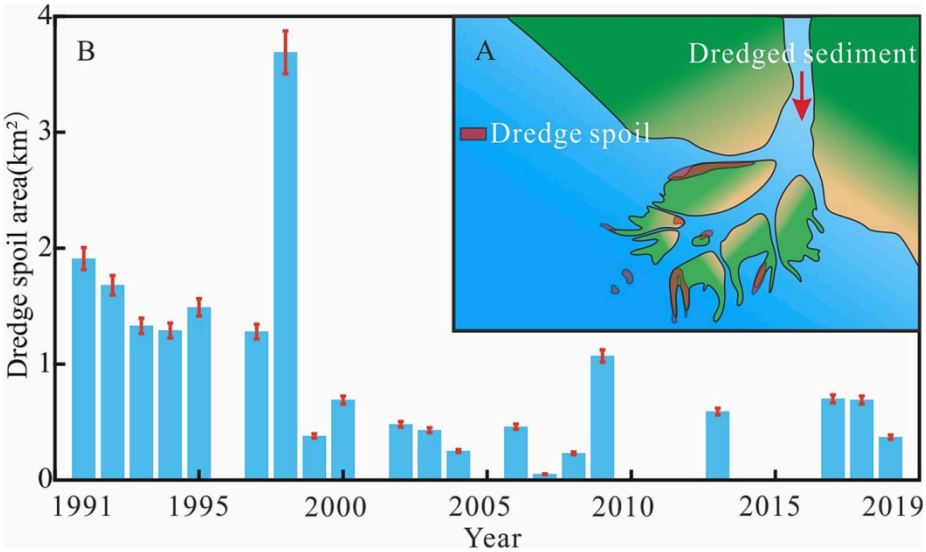

Fig. 11. Deltaic lands formed by dredge spoils in the AD. A. Dredge spoil model. The red polygons indicated the newly formed deltaic lands due to the dredge spoils. B. Deltaic lands formed by dredge spoils in the AD from 1991 to 2019. Dredging spoil land area from 1991 to 2017 was collected by Zhang et al. (2021).

that the deltas prograde in the gulf with a constant slope, we could underestimate the risk of drowning. In order to accurately judge the impact of SLR on deltaic islands, more accretion data are required.

4.4. Anthropogenic activities

Human activities have the potential to alter and exert a dominant influence on the evolution of deltaic islands (Allen et al., 2012; Carle et al., 2015; Elliton et al., 2020). In the WLD, neither human settlements nor direct manipulation (dredging or levees construction) has occurred since the formation of the delta. Only a few structures, houseboats and moorings exist in the northwestern area (Fig. S2). The system is therefore relatively natural, with a symmetric, lobate shape. The center of mass of the WLD has migrated seaward at a constant rate (Fig. 4P-R). In summary, under sufficient sediment supply and minor anthropogenic impacts, deltaic islands are subject to uniform expansion and a vertical accretion that conserves the topset slope (Fig. 4, Fig. 10B).

Unlike the WLD, the growth of the AD was highly affected by dredging activities (Zhang et al., 2021, Fig. 11A). To meet navigation requirements, the USACE has dredged the sediment deposited in the ARMC and used it to create new wetlands since 1975 (Allen et al., 2012). Zhang et al. (2021) found that dredge spoil activities has created about 19.48 km^2 of deltaic lands in AD from 1985 to 2017. Using visual interpretation, we found that the new deltaic island area formed by dredge spoils was 0.69 km^2 in 2018 and 0.37 km^2 2019 (Fig. 11B). The significant westward expansion of deltaic island in the AD during 1991–1999 is probably due to extensive spoil deposition on the western delta. Wetland construction slowed down in the subsequent years and thus generated a slower expansion of the islands (Fig. 5). Therefore, spoil disposal has altered the natural evolution of the AD, and also disturbed the natural migration of the center of mass. The artificially formed islands might not accrete fast enough to offset sea-level rise. The slow accretion might also prevent the maintenance of a constant topset slope in the AD.

5. Conclusion

As one of the few deltaic areas expanding seaward, the islands in the ARDC are of great significance to the study of coastal land restoration. Here, we analyzed the temporal and spatial variations of the deltaic islands in WLD and AD between 1991 and 2019. We identified possible drivers for deltaic island evolution. The main conclusions are as follows:

1) The area of deltaic island in the ARDC exhibited a substantial increase with a rate of 1.29 km^2/yr from 1991 to 2019. The deltaic islands area of WLD and AD expanded with an increasing rate of 0.60 km^2/yr and 0.69 km^2/yr, respectively. The increasing rate of AD is slightly higher than that of WLD, which can be explained by the dredging and disposal activities in AD that provided extra material for the growth of deltaic islands. The WP, CP, and EP of WLD expanded seawards at the rate of 26 m/yr, 45 m/yr, 19 m/yr, The WP, CP, and EP of AD prograded 25 m/yr, 43 m/yr and 1 m/yr. The higher progradation rates of the central parts indicate that the two deltas are elongating in Atchafalaya Bay, with a shape typical of fluvial dominated deltas;
2) Fluvial SSD and peak discharge events triggered the expansion and dominated the spatial evolution pattern of deltaic island in WLD. Anthropogenic activities have altered the natural growth pattern of deltaic island in the AD, and disposal of dredged sediment can be responsible for the expansion of the delta;
3) Hurricane and tropical storm events caused mainly erosive impacts on the WLD, but transient erosion or siltation on the AD and high-intensity hurricanes that made landfall east of the delta caused more erosion on the AD. Assuming that the deltas prograde in the gulf with a constant slope, the deltaic islands of ARDC are not facing threat of sea level inundation, as the rate of vertical accretion was higher than SLR, except for the EP of AD may be at risk of drowning.

CRediT authorship contribution statement

Jiangjie Yang: Conceptualization, Methodology, Investigation, Software, Visualization, Writing – original draft. **Zhijun Dai:** Conceptualization, Supervision, Investigation. **Yaying Lou:** Methodology, Software, Visualization. **Xuefei Mei:** Conceptualization, Supervision. **Sergio Fagherazzi:** Conceptualization, Writing – review & editing.

Declaration of Competing Interest

The authors declare that they have no known competing financial interests or personal relationships that could have appeared to influence the work reported in this paper.

Data availability

Data will be made available on request.

Acknowledgement

This research was supported by the Joint Key Funds of National Natural Science Foundation of China (U2040202), the Key Projects of Intergovernmental Science and Technology Innovation Cooperation of the Ministry of Science and Technology in China (2018YFE0109900), and the USA National Science Foundation awards 1637630 (PIE LTER) and 1832221 (VCR LTER).

Appendix A. Supplementary data

Supplementary data to this article can be found online at https://doi.org/10.1016/j.jhydrol.2023.129814.

References

Allen, Y.C., Couvillion, B.R., Barras, J.A., 2012. Using multitemporal remote sensing imagery and inundation measures to improve land change estimates in coastal wetlands. Estuar. Coasts 35 (1), 190–200.

Anthony, E.J., Brunier, G., Besset, M., Goichot, M., Dussouillez, P., Nguyen, V.L., 2015. Linking rapid erosion of the Mekong River delta to human activities. Sci. Rep. 5, 14745.

Barras, J.A., 2003. Changes to Cote Blanche Hydrologic Restoration (TV-04) Area After Hurricane Lili. U.S. Geological Survey, National Wetlands Research Center, Map ID USGS NWRC 2.

Barras, J.A., 2007. Land area changes in coastal Louisiana after Hurricanes Katrina and Rita. In: Farris, G.S., Smith, G.J., Crane, M.P., Demas, C.R., Robbins, L.L., Lavoie, D. L. (Eds.), Science and the Storms-The USFS Response to the Hurricanes of 2005. U.S. Geological Survey Circular 1306, pp. 98-113.

Belgiu, M., Dr̆agut, L., 2016. Random forest in remote sensing: A review of applications and future directions. ISPRS J. Photogramm. Remote Sens. 114, 24–31.

Bevington, A.E., Twilley, R.R., Sasser, C.E., Holm, G.O., 2017. Contribution of river floods, hurricanes, and cold fronts to elevation change in a prograding deltaic floodplain in the northern Gulf of Mexico, USA. Estuar. Coast. Shelf Sci. 191, 188–200.

Bwangoy, J.-R., Hansen, M.C., Roy, D.P., Grandi, G.D., Justice, C.O., 2010. Wetland mapping in the Congo Basin using optical and radar remotely sensed data and derived topographical indices. Remote Sens. Environ. 114 (1), 73–86.

Carle, M.V., Sasser, C.E., Roberts, H.H., 2015. Accretion and vegetation community change in the wax lake delta following the historic 2011 Mississippi River flood. J. Coast. Res. 31 (3), 569–587.

Carle, M., Sasser, C., 2015. Productivity and Resilience: Long-Term Trends and Storm-Driven Fluctuations in the Plant Community of the Accreting Wax Lake Delta. Estuar. Coasts 39 (2), 406–422.

Chen, B., Xiao, X., Li, X., Pan, L., Doughty, R., Ma, J., Dong, J., Qin, Y., Zhao, B., Wu, Z., Sun, R., Lan, G., Xie, G., Clinton, N., Giri, C., 2017. A mangrove forest map of china in 2015: analysis of time series landsat 7/8 and sentinel-1a imagery in google earth engine cloud computing platform. ISPRS J. Photogramm. Remote Sens. 131, 104–120.

Costanza, R., Pérez-Maqueo, O., Martinez, M.L., Sutton, P., Anderson, S.J., Mulder, K., 2008. The value of coastal wetlands for hurricane protection, AMBIO: A. J. Human Environment 37 (4), 241–248.

Dai, Z., Liu, J., Fu, G., Xie, H., 2013. A thirteen-year record of bathymetric changes in the North passage, Changjiang (Yangtze) estuary. Geomorphology 187, 101–107.

Dai, Z., Mei, X., Darby, S.E., Lou, Y., Li, W., 2018. Fluvial sediment transfer in the Changjiang (Yangtze) river-estuary depositional system. J. Hydrol. 566, 719–734.

Dai Z., 2021. Changjiang riverine and estuarine hydro-morphodynamic processes,In the Context of Anthropocene Era. Springer Press.

DeLaune, R.D., Sasser, C.E., Evers-Hebert, E., White, J.R., Roberts, H.H., 2016. Influence of the Wax Lake Delta sediment diversion on aboveground plant productivity and carbon storage in deltaic island and mainland coastal marshes. Estuarine Coast and Shelf Science 177, 83–89.

Elliton, C., Xu, K., Rivera-Monroy, V.H., 2020. The Impact of Biophysical Processes on Sediment Transport in the Wax Lake Delta (Louisiana, USA). Water 12, 2072.

Ericson, J.P., Vörösmarty, C.J., Dingman, L., Ward, L.G., Meybeck, M., 2006. Effective sea-level rise and deltas: Causes of change and human dimension implications. Global Planet. Change 50 (1), 63–82.

Fagherazzi, S., Edmonds, D.A., Nardin, W., Leonardi, N., Canestrelli, A., Falcini, F., Jerolmack, D.J., Mariotti, G., Rowland, J.C., Slingerland, R.L., 2015. Dynamics of river mouth deposits. Rev. Geophys. 53 (3), 642–672.

Fagherazzi, S., Mariotti, G., Leonardi, N., Canestrelli, A., Nardin, W., & Kearney, W. S., 2020. Salt marsh dynamics in a period of accelerated sea level rise. Journal of Geophysical Research: Earth Surface, 125, e2019JF005200.

Farda, N.M., 2017. Multi-temporal Land Use Mapping of Coastal Wetlands Area using Machine Learning in Google Earth Engine. IOP Conf. Ser.: Earth Environ. Sci. 98 (1), 012042.

FitzGerald, S.M., 1998. Sand body geometry of the Wax Lake Outlet delta, Atchafalaya Bay. Louisiana State University, Baton Rouge, Louisiana, Louisiana.

Fu, Y.u., Cao, W., Pan, D., Ren, Y.u., 2022. Changes of groundwater arsenic risk in different seasons in Hetao Basin based on machine learning model. Sci. Total Environ. 817, 153058.

Geleynse, N., Hiatt, M., Sangireddy, H., Passalacqua, P., 2015. Identifying environmental controls on the shoreline of a natural river delta. J. Geophys. Res. Earth 120 (5), 877–893.

Gorelick, N., Hancher, M., Dixon, M., Ilyushchenko, S., Thau, D., Moore, R., 2017. Google Earth Engine: planetary-scale geospatial analysis for everyone. Remote Sens. Environ. 202, 18–27.

Guntenspergen, G.R., Cahoon, D.R., Grace, J., Steyer, G.D., Fournet, S., Townson, M.A., Foote, A.L., 1995. Disturbance and recovery of the Louisiana coastal marsh landscape from the impacts of Hurricane Andrew. Journal of Coastal Research, Special Issue No. 21, 324–339.

Guo, H., Huang, J.J., Zhu, X., Wang, B.o., Tian, S., Xu, W., Mai, Y., 2021. A generalized machine learning approach for dissolved oxygen estimation at multiple spatiotemporal scales using remote sensing. Environ. Pollut. 288, 117734.

Guo, B., Zang, W., Han, B., Yang, F., Luo, W., He, T., Fan, Y., Yang, X., Chen, S., 2020. Dynamic monitoring of desertification in Naiman Banner based on feature space models with typical surface parameters derived from LANDSAT images. Land Degrad. Dev. 31 (12), 1573–1592.

Horowitz, A.J., 2010. A quarter century of declining suspended sediment fluxes in the Mississippi River and the effect of the 1993 flood. Hydrol. Process. 24, 13–34.

Howes, N.C., FitzGerald, D.M., Hughes, Z.J., Georgiou, I.Y., Kulp, M.A., Miner, M.D., Smith, J.M., Barras, J.A., 2010. Hurricane-induced failure of low salinity wetlands. Proc. Natl. Acad. Sci. U.S.A. 107 (32), 14014–14019.

Huete, A., Didan, K., Miura, T., Rodriguez, E.P., Gao, X., Ferreira, L.G., 2002. Overview of the radiometric and biophysical performance of the MODIS vegetation indices. Remote Sens. Environ. 83 (1-2), 195–213.

Jankowski, K., To ̈rnqvist, T., Fernandes, A., 2017. Vulnerability of Louisiana's coastal wetlands to present-day rates of relative sea-level rise. Nature Communication, 8, 14792.

Keim, B.D., Muller, R.A., Stone, G.W., 2007. Spatiotemporal patterns and return periods of tropical storm and hurricane strikes from Texas to Maine. J. Clim. 20, 3498–3509.

Kirwan, M.L., Megonigal, J.P., 2013. Tidal wetland stability in the face of human impacts and sea-level rise. Nature 504 (7478), 53–60.

Kopp, R.E., DeConto, R.M., Bader, D.A., Hay, C.C., Horton, R.M., Kulp, S., Oppenheimer, M., Pollard, D., Strauss, B.H., 2017. Evolving understanding of antarctic ice-sheet physics and ambiguity in probabilistic sea-level projections. Earth's Future 5 (12), 1217–1233.

Kumar, P., Dobriyal, M., Kale, A., Pandey, A.K., 2021. Temporal dynamics change of land use/land cover in Jhansi district of Uttar Pradesh over past 20 years using LANDSAT TM, ETM+ and OLI sensors. Remote Sens. Appl.: Soc. Environ. 23, 100579.

Lamb, M.P., Nittrouer, J.A., Mohrig, D., Shaw, J., 2012. Backwater and river plume controls on scour upstream of river mouths: Implications for fluvio-deltaic morphodynamics. J. Geophys. Res. Earth 117 (F1), n/a–n/a.

Lawrence, R.L., Wrlght, A., 2001. Rule-based classification systems using classification and regression tree (cart) analysis. Photogrammetric Engineering & Remote Sensing, 2001,67(10), 1137-1142.

Li, Z., Guo, X., 2010. A suitable vegetation index for quantifying temporal variation of leaf area index (LAI) in semiarid mixed grassland. Can. J. Remote. Sens. 36 (6), 709–721.

Long, C., Dai, Z., Zhou, X., Mei, X., Mai Van, C., 2021. Mapping mangrove forests in the Red River Delta. Vietnam. Forest Ecology and Management 483, 118910.

Long, C., Dai, Z., Wang, R., Lou, Y., Zhou, X., Li, S., Nie, Y., 2022. Dynamic changes in mangroves of the largest delta in northern Beibu Gulf. For. Ecol. Manage. 504, 119855.

Lou, Y., Dai, Z., Long, C., Dong, H., Wei, W., Ge, Z., 2022. Image-based machine learning for monitoring the dynamics of the largest salt marsh in the Yangtze River Delta. J. Hydrol. 608, 127681.

Magidi, J., Nhamo, L., Mpandeli, S., Mabhaudhi, T., 2021. Application of the Random Forest Classifier to Map Irrigated Areas Using Google Earth Engine. Remote Sens. (Basel) 13 (5), 876.

Meng, X., Gao, X., Li, S., Lei, J., 2020. Spatial and temporal characteristics of vegetation NDVI changes and the driving forces in Mongolia during 1982–2015. Remote Sens. (Basel) 12, 603.

Mossa, J., Roberts, H.H., 1990. Synergism of riverine and winter storm-related sediment transport processes in Louisiana's coastal wetlands. AAPG Bull. 40.

Na, R., Du, H., Na, L.i., Shan, Y., He, H.S., Wu, Z., Zong, S., Yang, Y., Huang, L., 2019. Spatiotemporal changes in the Aeolian desertification of Hulunbuir Grassland and its driving factors in China during 1980–2015. Catena 182, 104123.

Nardin, W., Edmonds, D.A., Fagherazzi, S., 2016. Influence of vegetation on spatial patterns of sediment deposition in deltaic islands during flood. Adv. Water Resour. 93, 236–248.

Nienhuis, J.H., Ashton, A.D., Edmonds, D.A., Hoitink, A.J.F., Kettner, A.J., Rowland, J. C., Törnqvist, T.E., 2020. Global-scale human impact on delta morphology has led to net land area gain. Nature 577 (7791), 514–518.

Nittrouer, J.A., Allison, M.A., Campanella, R., 2008. Bedform transport rates for the lowermost Mississippi River. J. Geophys. Res. 113, 1–16.

Nittrouer, J.A., Mohrig, D., Allison, M.A., 2011. Punctuated sand transport in the lowermost Mississippi River. J. Geophys. Res. 116 (F4), F04025.

Nittrouer, J.A., Shaw, J., Lamb, M.P., Mohrig, D., 2012. Spatial and temporal trends for water-flow velocity and bed-material sediment transport in the lower Mississippi River. Geol. Soc. Am. Bull. 124 (3–4), 400–414.

Nyman, J.A., Crozier, C.R., DeLaune, R.D., 1995. Roles and patterns of hurricane sedimentation in an estuarine marsh landscape. Estuar. Coast. Shelf Sci. 40 (6), 665–679.

Olliver, E. A., & Edmonds, D. A., 2021. Hydrological connectivity controls magnitude and distribution of sediment deposition within the deltaic islands of Wax Lake Delta, LA, USA. Journal of Geophysical Research: Earth Surface, 126, e2021JF006136.

Olliver, E.A., Edmonds, D.A., Shaw, J.B., 2020. Influence of Floods, Tides, and Vegetation on Sediment Retention in Wax Lake Delta, Louisiana, USA. J. Geophys. Res. Earth Surf. 125 (1).
Olson, K.R., Suski, C.D., 2021. Mississippi River Delta: Land Subsidence and Coastal Erosion. Open J. Soil Sci. 11 (03), 139–163.
Pertiwi, A.P., Roth, A., Schaffhauser, T., Bhola, P.K., Reuß, F., Stettner, S., Kuenzer, C., Disse, M., 2021. Monitoring the Spring Flood in Lena Delta with Hydrodynamic Modeling Based on SAR Satellite Products. Remote Sens. (Basel) 13, 4695.
Reeve, D.E., Karunarathna, H., 2009. On the prediction of long-term morphodynamic response of estuarine systems to sea level rise and human interference. Cont. Shelf Res. 29 (7), 938–950.
Roberts, H.H., Adams, R.D., Cunningham, R.H.W., 1980. Evolution of sand-dominant subaerial phase, Atchafalaya Delta, Louisiana. Am. Assoc. Pet. Geol. Bull. 64 (2), 264–279.
Roberts, H.H., Coleman, J.M., Bentley, S.J., Walker, N., 2003. An embryonic major delta lobe: A new generation of delta studies in the Atchafalaya-Wax Lake Delta system. Gulf Coast Assoc. Geol. Soc. Trans. 53, 690–703.
Rosen, T., Xu, Y.J., 2013. Recent decadal growth of the Atchafalaya River Delta complex: Effects of variable riverine sediment input and vegetation succession. Geomorphology 194 (4), 108–120.
Rouse, J.W, Haas, R.H., Scheel, J.A., Deering, D.W., 1974. Monitoring Vegetation Systems in the Great Plains with ERTS. Proceedings, 3rd Earth Resource Technology Satellite (ERTS) Symposium, 1, 48-62.
Sendrowski, A., Passalacqua, P., Castanedamoya, E., Twilley, R., 2016. Linking hydrologic connectivity and nutrient dynamics in a deltaic island of prograding Wax Lake Delta, coastal Louisiana. AGU Fall Meeting Abstracts.
Shaw, J.B., Mohrig, D., 2014. The importance of erosion in distributary channel network growth, Wax Lake Delta, Louisiana, USA. Geology 42 (1), 31–34.
Shlemon, R.J., 1975. Subaqueous delta formation-Atchafalaya Bay, Louisiana. In: Broussard, M.L. (Ed.), Deltas: Models of Exploration. Houston Geological Society, Houston, TX, pp. 209–221.
Sweet W. V., Kopp R. E., Weaver C. P., et al, 2017. Global and regional sea level rise scenarios for the United States.
Syvitski, J.P.M., Kettner, A.J., Overeem, I., Hutton, E.W.H., Hannon, M.T., Brakenridge, G.R., Day, J., Vorosmarty, C., Saito, Y., Giosan, L., Nicholls, R.J., 2009. Sinking deltas due to human activities. Nat. Geosci. 2 (10), 681–686.
Tang, M., Xu, Y.J., Xu, W., Wang, B.o., Cheng, H., 2021. Three-decadal erosion and deposition of channel bed in the Lower Atchafalaya River, the largest distributary of the Mississippi River. Geomorphology 380, 107638.
Turner, R.E., Baustian, J.J., Swenson, E.M., Spicer, J.S., 2006. Wetland sedimentation from hurricanes Katrina and Rita. Science 314 (5798), 449–452.
van Heerden, I.L., Roberts, H.H., 1988. Facies development of Atchafalaya Delta, Louisiana: a modern bayhead delta. Am. Assoc. Pet. Geol. Bull. 72 (4), 439–453.
Wagner, W., Lague, D., Mohrig, D., Passalacqua, P., Shaw, J., Moffett, K., 2017. Elevation change and stability on a prograding delta. Geophys. Res. Lett. 44, 1786–1794.
Walker, N.D., 2001. Tropical storm and hurricane wind effects on water level, salinity, and sediment transport in the river-influenced Atchafalaya-Vermilion Bay system, Louisiana, USA. Estuaries 24 (4), 498–508.
Wang, B., Xu, Y.J., Xu, W., Cheng, H.Q., Chen, Z.Y., Zhang, W.G., 2020. Channel bed dynamics below a large engineering-controlled river confluence - The uppermost Atchafalaya River, USA. Water 12, 2139.
Xiao, X., Hollinger, D., Aber, J., Goltz, M., Davidson, E.A., Zhang, Q., Moore, B., 2004. Satellite-Based Modeling of Gross Primary Production in an Evergreen Needleleaf Forest. Remote Sens. Environ. 89 (4), 519–534.
Xing, F., Syvitski, J.P.M., Kettner, A.J., Meselhe, E.A., Atkinson, J.H., Khadka, A.K., Chadwick, O., Ranaud, F., 2017. Morphological responses of the Wax Lake Delta, Louisiana, to Hurricanes Rita. Elem. Sci. Anth. 5.
Xu, H., 2006. Modification of normalized difference water index (NDWI) to enhance open water features in remotely sensed imagery. Int. J. Remote Sens. 27 (14), 3025–3033.
Xu, Y.J., 2010. Long-term Sediment Transport and Delivery of the Largest Distributary of the Mississippi River, the Atchafalaya, USA. In: Banasik, K., Horowitz, A., Owens, P. N., Stone, M., Walling, D.E. (Eds.), Sediment Dynamics for a Changing Future, 337. IAHS Publication, Wallingford, UK, pp. 282–290.
Xu, Y.J., Bryantmason, A., 2011. Determining the Nitrate Contribution of the Red River to the Atchafalaya River in the Northern Gulf of Mexico under Changing Climate. In: Peters, J. (Ed.), Water Quality: Current Trends and Expected Climate Change Impacts, 348. IAHS Publication, Wallingford, UK, pp. 95–100.
Xu, Z.-H., Wu, S.-H., Liu, M.-C., Zhao, J.-S., Chen, Z.-H., Zhang, K.e., Zhang, J.-J., Liu, Z., 2021. Effects of water discharge on river-dominated delta growth. Pet. Sci. 18 (6), 1630–1649.
Yang, H.F., Yang, S.L., Li, B.C., Wang, Y.P., Wang, J.Z., Zhang, Z.L., Xu, K.H., Huang, Y. G., Shi, B.W., Zhang, W.X., 2021. Different fates of the Yangtze and Mississippi deltaic wetlands under similar riverine sediment decline and sea-level rise. Geomorphology 381, 107646.
Zhang, L., Hu, Q., Tang, Z., 2022. Assessing the contemporary status of Nebraska's eastern saline wetlands by using a machine learning algorithm on the Google Earth Engine cloud computing platform. Environ. Monit. Assess. 194 (4), 193.
Zhang, X., Xu, K., Yang, Z., Tan, X., Wu, C., 2021. Decreasing land growth and unique seasonal area fluctuations of two newborn Mississippi subdeltas. Geomorphology 378 (1), 107617.
Zhou, X., Dai, Z., Mei, X., 2020. The multi-decadal morphodynamic changes of the mouth bar in a mixed fluvial-tidal estuarine channel. Mar. Geol. 429, 106311.
Zou, Z.H., Dong, J.W., Menarguez, M.A., Xiao, X.M., Qin, Y.W., Doughty, R.B., Hooker, K.V., Hambright, K.D., 2017. Continued decrease of open surface water body area in Oklahoma during 1984–2015. Sci. Total Environ. 595, 451–460.